

Nonheme Oxoiron(IV) Complexes of Tris(2-pyridylmethyl)amine with *cis*-Monoanionic LigandsJan-Uwe Rohde,^{†‡} Audria Stubna,[§] Emile L. Bominaar,[§] Eckard Münck,^{*,§} Wonwoo Nam,^{*,||} and Lawrence Que, Jr.^{*,†}*Department of Chemistry and Center for Metals in Biocatalysis, University of Minnesota, Minneapolis, Minnesota 55455, Department of Chemistry, Carnegie Mellon University, Pittsburgh, Pennsylvania 15213, and Department of Chemistry, Division of Nano Sciences, and Center for Biomimetic Systems, Ewha Womans University, Seoul 120-750, Korea*

Received May 1, 2006

Treatment of $[\text{Fe}^{\text{IV}}(\text{O})(\text{TPA})(\text{NCMe})(\text{CF}_3\text{SO}_3)_2]$ [TPA, *N,N,N*-tris(2-pyridylmethyl)amine] with 3 equiv of NR_4X ($\text{X} = \text{CF}_3\text{CO}_2$, Cl , or Br) in MeCN at -40°C affords a series of metastable $[\text{Fe}^{\text{IV}}(\text{O})(\text{TPA})(\text{X})]^+$ complexes. Some characteristic features of the $S = 1$ oxoiron(IV) unit are quite insensitive to the ligand substitution in the equatorial plane, namely, the Fe–O distances (1.65–1.66 Å), the energy (~ 7114.5 eV) and intensity [25(2) units] of the 1s-to-3d transition in the X-ray absorption spectra, and the Mössbauer isomer shifts (0.01–0.06 $\text{mm}\cdot\text{s}^{-1}$) and quadrupole splittings (0.92–0.95 $\text{mm}\cdot\text{s}^{-1}$). The coordination of the anionic X ligand, however, is evidenced by red shifts of the characteristic near-IR ligand-field bands (720–800 nm) and spectroscopic observation of the bound anion by ^{19}F NMR for $\text{X} = \text{CF}_3\text{CO}_2$ and by EXAFS analysis for $\text{X} = \text{Cl}$ ($r_{\text{Fe}-\text{Cl}} = 2.29$ Å) and Br ($r_{\text{Fe}-\text{Br}} = 2.43$ Å). Density functional theory calculations yield Mössbauer parameters and bond lengths in good agreement with the experimental data and produce excited-state energies that follow the trend observed in the ligand-field bands. Despite mitigating the high effective charge of the iron(IV) center, the substitution of the MeCN ligand with monoanionic ligands X^- decreases the thermal stability of $[\text{Fe}^{\text{IV}}(\text{O})(\text{TPA})]^{2+}$ complexes. These anion-substituted complexes model the *cis*- $\text{X}-\text{Fe}^{\text{IV}}=\text{O}$ units proposed in the mechanisms of oxygen-activating nonheme iron enzymes.

Introduction

Proposed mechanisms for the activation of dioxygen by nonheme monoiron enzymes often involve a high-valent oxoiron intermediate that is responsible for the substrate oxidation step.^{1–3} Recently, the first such species was identified in the catalytic cycle of the 2-oxoglutarate-dependent monoiron enzyme TauD and characterized as having an $S = 2$ iron(IV) center with a terminal $\text{Fe}^{\text{IV}}=\text{O}$

unit.^{4–9} Within the same time frame, the first synthetic examples of mononuclear nonheme oxoiron(IV) complexes were reported and extensively characterized by a variety of spectroscopic techniques.^{10–16} In general, these intermediates

* To whom correspondence should be addressed. E-mail: em40@andrew.cmu.edu (E.M.), wwnam@ewha.ac.kr (W.N.), que@chem.umn.edu (L.Q.).

[†] University of Minnesota.

[‡] Current address: Department of Chemistry, The University of Iowa, Iowa City, IA 52242.

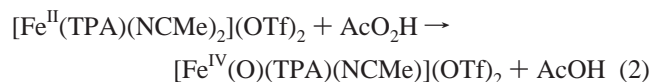
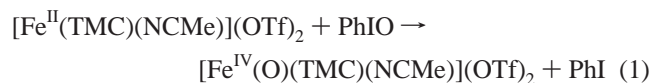
[§] Carnegie Mellon University.

^{||} Ewha Womans University.

- (1) Solomon, E. I.; Brunold, T. C.; Davis, M. I.; Kemsley, J. N.; Lee, S.-K.; Lehnert, N.; Neese, F.; Skulan, A. J.; Yang, Y.-S.; Zhou, J. *Chem. Rev.* **2000**, *100*, 235–349.
- (2) Costas, M.; Mehn, M. P.; Jensen, M. P.; Que, L., Jr. *Chem. Rev.* **2004**, *104*, 939–986.
- (3) Abu-Omar, M. M.; Loaiza, A.; Hontzeas, N. *Chem. Rev.* **2005**, *105*, 2227–2252.

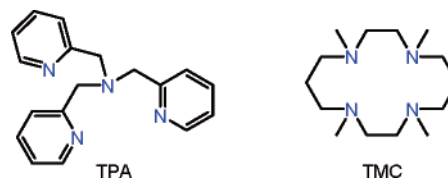
- (4) Price, J. C.; Barr, E. W.; Tirupati, B.; Bollinger, J. M., Jr.; Krebs, C. *Biochemistry* **2003**, *42*, 7497–7508.
- (5) Price, J. C.; Barr, E. W.; Glass, T. E.; Krebs, C.; Bollinger, J. M., Jr. *J. Am. Chem. Soc.* **2003**, *125*, 13008–13009.
- (6) Proshlyakov, D. A.; Henshaw, T. F.; Monterosso, G. R.; Ryle, M. J.; Hausinger, R. P. *J. Am. Chem. Soc.* **2004**, *126*, 1022–1023.
- (7) Riggs-Gelasco, P. J.; Price, J. C.; Guyer, R. B.; Brehm, J. H.; Barr, E. W.; Bollinger, J. M., Jr.; Krebs, C. *J. Am. Chem. Soc.* **2004**, *126*, 8108–8109.
- (8) Bollinger, J. M., Jr.; Price, J. C.; Hoffart, L. M.; Barr, E. W.; Krebs, C. *Eur. J. Inorg. Chem.* **2005**, 4245–4254.
- (9) Krebs, C.; Price, J. C.; Baldwin, J.; Saleh, L.; Green, M. T.; Bollinger, J. M., Jr. *Inorg. Chem.* **2005**, *44*, 742–757.
- (10) Grapperhaus, C. A.; Mienert, B.; Bill, E.; Weyhermüller, T.; Wieghardt, K. *Inorg. Chem.* **2000**, *39*, 5306–5317.
- (11) Rohde, J.-U.; In, J.-H.; Lim, M. H.; Brennessel, W. W.; Bukowski, M. R.; Stubna, A.; Münck, E.; Nam, W.; Que, L., Jr. *Science* **2003**, *299*, 1037–1039.
- (12) Lim, M. H.; Rohde, J.-U.; Stubna, A.; Bukowski, M. R.; Costas, M.; Ho, R. Y. N.; Münck, E.; Nam, W.; Que, L., Jr. *Proc. Natl. Acad. Sci. U.S.A.* **2003**, *100*, 3665–3670.

were generated by reaction of the respective iron(II) precursors with stoichiometric amounts of oxygen atom donors (eqs 1 and 2). Two of these have been structurally characterized by X-ray crystallography,^{11,17} while EXAFS analysis has provided structural insight for many of the other complexes that have not yet been crystallized.^{12,15,16,18,19} High-field Mössbauer investigations of several of these complexes show that the oxoiron(IV) center is low spin ($S = 1$),^{10–13,15,16} while magnetic circular dichroism (MCD) studies of $[\text{Fe}^{\text{IV}}(\text{O})(\text{TMC})(\text{NCMe})]^{2+}$ establish that the characteristic near-IR features associated with this class of compounds derive from ligand-field transitions of the oxoiron(IV) unit.²⁰



Structural biological, spectroscopic, and mechanistic evidence indicates that carboxylate and other anionic ligands can be coordinated to the metal center in the catalytic cycles of various nonheme monoiron enzymes.^{1–3} Most oxygen-activating nonheme monoiron enzymes share a common 2-His-1-carboxylate facial triad motif that binds the iron(II) in the active site.²¹ In 2-oxoglutarate-dependent enzymes, cofactor binding prior to oxygen activation introduces a second carboxylate ligand into the iron coordination sphere,²² and in a new subset of these enzymes called halogenases, a chloride ion is proposed to bind to the iron center before being transferred to the substrate.^{23,24} In the case of isopenicillin N synthase, the cysteine thiolate of its tripeptide substrate is coordinated to the iron(II) center in the enzyme—

Chart 1. Tetradentate Ligands TPA and TMC



substrate complex before it is oxidized by dioxygen to form the thiazolidine ring of isopenicillin.²⁵

Given that many of the synthetic oxoiron(IV) complexes characterized thus far have five neutral nitrogen ligands,^{11–15,17} we have sought to exchange the bound MeCN solvent with anions in the coordination spheres of oxoiron(IV) centers of tetradentate N4 ligands. With respect to $[\text{Fe}^{\text{IV}}(\text{O})(\text{TMC})(\text{NCMe})]^{2+}$, we recently reported evidence for the replacement of the trans MeCN ligand with trifluoroacetate,²⁶ azide,²⁷ thiocyanate,²⁷ and thiolate,¹⁶ resulting in shifts of the characteristic near-IR bands of the oxoiron(IV) unit as well as changes in the stability and reactivity of the oxoiron(IV) unit. Because of the topology of the tripodal *N,N,N*-tris(2-pyridylmethyl)amine (TPA) ligand (Chart 1), the corresponding $[\text{Fe}^{\text{IV}}(\text{O})(\text{TPA})(\text{NCMe})]^{2+}$ ($2-\text{NCMe}$) complex has a labile coordination site *cis* to the oxo ligand. Here, we report on ligand substitution studies of $2-\text{NCMe}$ with carboxylates and halides, affording complexes with *cis*-X- $\text{Fe}^{\text{IV}}=\text{O}$ moieties, and describe the influence of the equatorial ligand field on the spectroscopic properties of the oxoiron(IV) unit. As a followup to our initial report,¹² a more detailed discussion of the conditions required for the formation of $2-\text{NCMe}$ is included.

Experimental Section

Materials and General Procedures. All reagents and solvents were purchased from commercial sources and were used as received, unless noted otherwise. Solvents were dried according to published procedures and distilled under argon prior to use.²⁸ Preparation and handling of air- and moisture-sensitive materials were carried out under an inert gas atmosphere by using either standard Schlenk and vacuum-line techniques or a glovebox. Elemental analyses were performed by Atlantic Microlab, Inc., Norcross, GA. $[\text{Fe}(\text{TPA})(\text{OTf})_2]$ ($1-\text{OTf}$) was synthesized according to a published procedure.¹² The preparation of $[\text{Fe}^{\text{IV}}(\text{O})(\text{TPA})(\text{OTf})_2]$ was carried out analogously by using $^{57}\text{Fe}(\text{OTf})_2 \cdot 2\text{MeCN}$.

$\text{NEt}_4[\text{FeCl}_4]$. $\text{NEt}_4[\text{FeCl}_4]$ was synthesized according to a published procedure.²⁹ Yellow single crystals were obtained upon recrystallization from dry MeOH at -20°C . The unit cell parameters of a crystal of this fraction were found to be identical with those published.²⁹ Anal. Calcd for $\text{C}_8\text{H}_{20}\text{Cl}_4\text{FeN}$: C, 29.30; H, 6.15; Cl, 43.25; N, 4.27. Found: C, 29.39; H, 6.18; Cl, 43.54;

- (13) Kaizer, J.; Klinker, E. J.; Oh, N. Y.; Rohde, J.-U.; Song, W. J.; Stubna, A.; Kim, J.; Münck, E.; Nam, W.; Que, L., Jr. *J. Am. Chem. Soc.* **2004**, *126*, 472–473.
- (14) Balland, V.; Charlot, M.-F.; Banse, F.; Girerd, J.-J.; Mattioli, T. A.; Bill, E.; Bartoli, J.-F.; Battioni, P.; Mansuy, D. *Eur. J. Inorg. Chem.* **2004**, 301–308.
- (15) Jensen, M. P.; Costas, M.; Ho, R. Y. N.; Kaizer, J.; Mairata i Payeras, A.; Münck, E.; Que, L., Jr.; Rohde, J.-U.; Stubna, A. *J. Am. Chem. Soc.* **2005**, *127*, 10512–10525.
- (16) Bukowski, M. R.; Koehntop, K. D.; Stubna, A.; Bominaar, E. L.; Halfen, J. A.; Münck, E.; Nam, W.; Que, L., Jr. *Science* **2005**, *310*, 1000–1002.
- (17) Klinker, E. J.; Kaizer, J.; Brennessel, W. W.; Woodrum, N. L.; Cramer, C. J.; Que, L., Jr. *Angew. Chem., Int. Ed.* **2005**, *44*, 3690–3694.
- (18) Rohde, J.-U.; Torelli, S.; Shan, X.; Lim, M. H.; Klinker, E. J.; Kaizer, J.; Chen, K.; Nam, W.; Que, L., Jr. *J. Am. Chem. Soc.* **2004**, *126*, 16750–16761.
- (19) Abbreviations used: OTf, trifluoromethylsulfonate or -triflate anion; TMC, 1,4,8,11-tetramethyl-1,4,8,11-tetraazacyclotetradecane or tetra-(*N*-methyl)cyclam; TPA, *N,N,N*-tris(2-pyridylmethyl)amine; EXAFS, extended X-ray absorption fine structure; XANES, X-ray absorption near-edge structure; XAS, X-ray absorption spectroscopy.
- (20) Decker, A.; Rohde, J.-U.; Que, L., Jr.; Solomon, E. I. *J. Am. Chem. Soc.* **2004**, *126*, 5378–5379.
- (21) Koehntop, K. D.; Emerson, J. P.; Que, L., Jr. *J. Biol. Inorg. Chem.* **2005**, *10*, 87–93.
- (22) Schofield, C. J.; Zhang, Z. *Curr. Opin. Struct. Biol.* **1999**, *9*, 722–731.
- (23) Vaillancourt, F. H.; Yin, J.; Walsh, C. T. *Proc. Natl. Acad. Sci. U.S.A.* **2005**, *102*, 10111–10116.
- (24) Vaillancourt, F. H.; Yeh, E.; Vosburg, D. A.; O'Connor, S. E.; Walsh, C. T. *Nature* **2005**, *436*, 1191–1194.

- (25) Burzlaff, N. I.; Rutledge, P. J.; Clifton, I. J.; Hensgens, C. M. H.; Pickford, M.; Adlington, R. M.; Roach, P. L.; Baldwin, J. E. *Nature* **1999**, *401*, 721–724.
- (26) Rohde, J.-U.; Que, L., Jr. *Angew. Chem., Int. Ed.* **2005**, *44*, 2255–2258.
- (27) Sastri, C. V.; Park, M. J.; Ohta, T.; Jackson, T. A.; Stubna, A.; Seo, M. S.; Lee, J.; Kim, J.; Kitagawa, T.; Münck, E.; Que, L., Jr.; Nam, W. *J. Am. Chem. Soc.* **2005**, *127*, 12494–12495.
- (28) Armarego, W. L. F.; Perrin, D. D. *Purification of Laboratory Chemicals*; Butterworth-Heinemann: Oxford, U.K., 1997.
- (29) Evans, D. J.; Hills, A.; Hughes, D. L.; Leigh, G. J. *Acta Crystallogr., Sect. C: Cryst. Struct. Commun.* **1990**, *C46*, 1818–1821.

N, 4.22. This material was used as a standard for the X-ray absorption spectroscopy (XAS) analysis of intermediates having Fe–Cl interactions (Supporting Information for XAS data of $\text{NET}_4[\text{FeCl}_4]$, Figures S7–S9).

$\text{NET}_4[\text{FeBr}_4]$. $\text{NET}_4[\text{FeBr}_4]$ was synthesized by a procedure adapted from that of $\text{NET}_4[\text{FeI}_4]$.³⁰ The synthesis was carried out under an argon atmosphere using Schlenk techniques to limit the introduction of moisture. A solution of 463 mg (2.2 mmol) of NET_4Br in 3 mL of dry MeOH was added to a suspension of 591 mg (2.0 mmol) of FeBr_3 in 4.5 mL of dry MeOH, affording an orange precipitate. For the purpose of providing an oxidative atmosphere, 0.2 mL (624 mg, 3.9 mmol) of Br_2 was added. The resulting mixture was vigorously stirred for 5 min and evacuated to dryness. The residue was dissolved in dry MeOH. Red single crystals suitable for X-ray diffraction were obtained upon standing at -20°C . Details of the crystal structure determination are described in the Supporting Information (Tables S5 and S6 and Figure S6). Further fractions of crystals were obtained upon successively reducing the volume of the red-brown solution. Anal. Calcd for $\text{C}_8\text{H}_{20}\text{Br}_4\text{FeN}$: C, 19.00; H, 3.99; Br, 63.20; N, 2.77. Found: C, 19.10; H, 3.84; Br, 63.54; N, 2.73. This material was used as a standard for the XAS analysis of intermediates having Fe–Br interactions (Supporting Information for XAS data of $\text{NET}_4[\text{FeBr}_4]$, Figures S7–S9).

Ligand-Exchange Reactions of $[\text{Fe}(\text{O})(\text{TPA})(\text{NCMe})](\text{OTf})_2$ [$2\text{--NCMe}(\text{OTf})_2$]. A 2 mM solution of **1**–OTf (0.004 mmol of Fe) in 2.0 mL of MeCN and 0.005 mL of H_2O (doubly deionized, Milli-Q Water System, Millipore, Bedford, MA) in a 1-cm UV–visible cuvette was precooled to -40°C . (Note: Dissolution of $[\text{Fe}(\text{TPA})(\text{OTf})_2]$ in MeCN readily afforded $[\text{Fe}(\text{TPA})(\text{NCMe})_2](\text{OTf})_2$ (**1**–NCMe(OTf)₂), as indicated by the ^{19}F NMR resonance of the free triflate ion in its NMR spectrum.) Addition of 1 equiv of AcO_2H (0.004 mmol, 32 wt % AcO_2H) in 0.05 mL of MeCN afforded **2**–NCMe(OTf)₂.¹² After **2**–NCMe was fully formed, 3 equiv (0.012 mmol) of the respective tetraalkylammonium salt ($\text{NET}_4\text{CF}_3\text{CO}_2$, NET_4AcO , NBu_4F , NBu_4Cl , NBu_4Br , or NBu_4I) in 0.05 mL of MeCN was added under stirring. ^{19}F NMR for **1**–OTf (CD_2Cl_2 , 282.4 MHz, -35°C): δ -52.2 (s, $[\text{Fe}(\text{TPA})(\text{OS}(\text{O})_2\text{CF}_3)_2]$). ^{19}F NMR for **1**–NCCD₃(OTf)₂ and **2**–NCCD₃(OTf)₂ (CD_3CN , 282.4 MHz, -35°C): δ -80.0 (s, CF_3SO_3^-). ^{19}F NMR for **2**– $\text{O}_2\text{CCF}_3(\text{OTf}) + \text{NET}_4\text{OTf} + \text{NET}_4\text{CF}_3\text{CO}_2$ (CD_3CN , 282.4 MHz, -35°C): δ -76 (s, CF_3CO_2^-), -80.0 (s, CF_3SO_3^-), -83.8 (s, $[\text{Fe}(\text{O})(\text{TPA})(\text{OC}(\text{O})\text{CF}_3)]^+$). For comparison, $[\text{Fe}(\text{TPA})(\text{OC}(\text{O})\text{CF}_3)(\text{NCMe})]\text{OTf}$ [**1**– $\text{O}_2\text{CCF}_3(\text{OTf})$] was generated from **1**–NCCD₃(OTf)₂ and 1 equiv of $\text{NET}_4\text{CF}_3\text{CO}_2$. ^{19}F NMR for **1**– $\text{O}_2\text{CCF}_3(\text{OTf}) + \text{NET}_4\text{OTf}$ (CD_3CN , 282.4 MHz, -35°C): δ -64.2 (s, $[\text{Fe}(\text{TPA})(\text{OC}(\text{O})\text{CF}_3)(\text{NCMe})]^+$), -80.0 (s, CF_3SO_3^-). ^{19}F NMR for $\text{NET}_4\text{CF}_3\text{CO}_2$ (CD_2Cl_2 , 282.4 MHz): δ -75.9 (s, CF_3CO_2^-). ^{19}F NMR for $\text{NET}_4\text{CF}_3\text{CO}_2$ (CD_3CN , 282.4 MHz): δ -75.8 (s, CF_3CO_2^-).

Sample Preparation for Mössbauer and XAS Studies. Samples of the substituted oxoiron(IV) complexes **2**– O_2CCF_3 , **2**–Cl, and **2**–Br were generated by the addition of the appropriate tetraalkylammonium salt to a solution of preformed **2**–NCMe as described below. Formation and conversion of the intermediates were followed by UV–visible–near-IR spectroscopy. After 5–10 min, ca. 0.5 mL of the solution with **2**– O_2CCF_3 , **2**–Cl, or **2**–Br was transferred into a precooled tandem Mössbauer/XAS cup, covered with Mylar tape, which was then submerged in liquid nitrogen.

$[\text{Fe}(\text{O})(\text{TPA})(\text{OC}(\text{O})\text{CF}_3)]^+ (\text{2--O}_2\text{CCF}_3)$. A solution of [^{57}Fe – $[\text{Fe}(\text{TPA})(\text{OTf})_2]$] and [^{57}Fe – $[\text{Fe}(\text{TPA})(\text{OTf})_2]$] (2:1, 0.0095 mmol of Fe) in 1.40 mL of MeCN was prepared in a 0.5-cm UV–visible cuvette and precooled to -40°C . A total of 1.1 equiv of AcO_2H (0.0104 mmol, 32 wt % AcO_2H) in 0.13 mL of MeCN was added. After **2**–NCMe was fully formed, 3 equiv of $\text{NET}_4\text{CF}_3\text{CO}_2$ (0.027 mmol) in 0.05 mL of MeCN was added.

$[\text{Fe}(\text{O})(\text{TPA})(\text{X})]^+$, **X = Cl (**2**–Cl) and Br (**2**–Br).** A solution of [^{57}Fe – $[\text{Fe}(\text{TPA})(\text{OTf})_2]$] and [^{57}Fe – $[\text{Fe}(\text{TPA})(\text{OTf})_2]$] (2:1, 0.009 mmol of Fe) in 1.5 mL of MeCN and 0.007 mL of H_2O (doubly deionized, Milli-Q Water System, Millipore, Bedford, MA) was prepared in a 0.5-cm UV–visible cuvette and precooled to -40°C . A total of 1.1 equiv of AcO_2H (0.010 mmol, 32 wt % AcO_2H) in 0.05 mL of MeCN was added. After **2**–NCMe was fully formed, $\text{NET}_4\text{Cl}\cdot x\text{H}_2\text{O}$ or NBu_4Br in 0.05 mL of MeCN was added: **2**–Cl, first sample, 4 equiv of NET_4Cl (0.036 mmol); **2**–Cl, second sample, 2.7 equiv of NET_4Cl (0.024 mmol); **2**–Br, 3 equiv of NBu_4Br (0.027 mmol).

$\text{NET}_4[\text{FeCl}_4]$ and $\text{NET}_4[\text{FeBr}_4]$. Solid samples of $\text{NET}_4[\text{FeCl}_4]$ and $\text{NET}_4[\text{FeBr}_4]$ were prepared by grinding the iron salt (1 mg) and boron nitride (99 mg) into a homogeneous mixture under a dry atmosphere. A total of 20 mg of the solid mixture was then packed into a sample plate (1-mm thickness) and covered with Mylar tape.

Physical Methods. UV–visible spectra were recorded on an HP 8453A diode-array spectrometer with samples maintained at low temperature using a cryostat from Unisoku Scientific Instruments, Osaka, Japan. ^{19}F NMR spectra were recorded on a Varian Inova VXR-300 or a Varian Inova VI-300 spectrometer at ambient temperature, unless noted otherwise. ^{19}F NMR chemical shifts (ppm) are reported referenced to an external standard, CFCl_3 (0 ppm). Mössbauer spectra were recorded with two spectrometers, using Janis Research Super-VariTemp dewars that allow studies in applied magnetic fields up to 8.0 T in the temperature range from 1.5 to 200 K. Mössbauer spectral simulations were performed using the WMOSS software package (WEB Research, Edina, MN). Isomer shifts are quoted relative to iron metal at 298 K.

XAS. Data Collection. XAS data were collected at the Stanford Synchrotron Radiation Laboratory (SSRL) of the Stanford Linear Accelerator Center, beamlines 7-3 and 9-3, and at the National Synchrotron Light Source (NSLS) of the Brookhaven National Laboratory, beamline X9B. Fe K-edge XAS data were recorded on frozen solutions at a constant temperature between 5 and 15 K over the energy range 6.9–8.0 keV as described previously.^{31,32} Storage ring conditions: 3 GeV, 50–100 mA (SSRL, SPEAR2); 2.8 GeV, 100–300 mA (NSLS). Contamination of higher harmonic radiation was minimized by detuning the Si(220) double-crystal monochromator by 50% at ~ 8 keV (beamline 7-3 at SSRL), by a bent focusing mirror (beamline 9-3 at SSRL), or by a harmonic rejection mirror (beamline X9B at NSLS). The horizontal spot size on the sample was 4–5 mm in most cases. Spectra were measured with 10 eV steps below the edge, 0.3 eV steps in the edge region, and steps equivalent to 0.05-Å⁻¹ increments above the edge [region borders were 6880, 7090, and 7140 eV at beamlines 7-3 and 9-3 (SSRL) and 6932, 7102, and 7137 eV at beamline X9B (NSLS)]. An iron foil spectrum was recorded concomitantly for internal energy calibration, and the first inflection point of the K-edge energy was assigned to 7112.0 eV. The data were obtained as fluorescence

(30) Pohl, S.; Saak, W. Z. *Naturforsch., B: Chem. Sci.* **1984**, 39B, 1236–1240.

(31) Scarrow, R. C.; Maroney, M. J.; Palmer, S. M.; Que, L., Jr.; Roe, A. L.; Salowe, S. P.; Stubbe, J. J. *Am. Chem. Soc.* **1987**, 109, 7857–7864.

(32) Shu, L.; Chiou, Y.-M.; Orville, A. M.; Miller, M. A.; Lipscomb, J. D.; Que, L., Jr. *Biochemistry* **1995**, 34, 6649–6659.

Table 1. Properties of $[\text{Fe}^{\text{IV}}(\text{O})(\text{TPA})(\text{X})]^{2+/+}$ Complexes, **2**–X, in This Study

	2 –NCMe ^a	2 –O ₂ CCF ₃	2 –Cl	2 –Br
λ_{max} (nm) (ϵ (M ⁻¹ cm ⁻¹))	724 (300)	745 (300)	778 (350)	800 (400)
$t_{1/2}$ at 10 °C	~1 h	~20 min	~2 min	~2 min
δ (mm·s ⁻¹) ^{b,c}	0.01 [0.07]	0.02 [0.08]	0.04 [0.08]	0.06 [0.09]
ΔE_Q (mm·s ⁻¹) ^{b,c}	0.92 [0.86]	0.92 [1.12]	0.95 [1.22]	0.95 [1.23]
η ^{b,c}	[0.7]	[0.7]	[0.5]	[0.4]
XAS preedge peak energy (eV) ^d	7114.4	7114.6	7114.5	7114.5
XAS preedge peak intensity ^d	25.4	26.7	24.6	24.5
$r_{\text{Fe-O}}$ (Å) ^c	1.65 [1.650]	1.66 [1.648]	1.65 [1.644]	1.66 [1.644]
$r_{\text{Fe-N}}$ (Å) ^c	1.98 [2.013]	1.98 [2.023]	1.98 [2.024]	1.98 [2.026]
$r_{\text{Fe-X}}$ (Å) ^c	1.98 [2.001]	1.98 [1.951]	2.29 [2.336]	2.43 [2.485]

^a From refs 12 and 18. ^b Isomer shifts have an error of ± 0.01 mm·s⁻¹, while quadrupole splittings have errors of ± 0.02 mm·s⁻¹. Experimental values for the asymmetry parameter η of the electric field gradient tensor have not yet been obtained. ^c Values in brackets were obtained from DFT calculations (see section V of Results section). ^d XAS preedge (1s \rightarrow 3d) peak energies and intensities (normalized on K edge) were determined by curve fitting to the data as described.^{36,42} Intensities are reported as peak areas (normalized to the edge jump) and were multiplied by 100. Because of the asymmetric shape of these features, a second peak at ~ 7117 eV of much lower intensity could be fit to the high-energy tail (Table S3 in the Supporting Information).

excitation spectra ($A_{\text{exp}} (C_{\text{f}}/C_0)$) using a solid-state germanium detector (Canberra).

The iron concentration in the samples and the number of scans acquired for each sample were as follows: **2**–O₂CCF₃, 6 mM Fe, 15 scans (beamline 9-3 at SSRL, SPEAR3, 24 detector elements); **2**–Cl, 6 mM Fe, 2 independent samples, 9 scans, 10 scans (beamline 7-3 at SSRL, SPEAR2, 20 detector elements); **2**–Br, 6 mM Fe, 13 scans (beamline 7–3 at SSRL, SPEAR2, 20 detector elements); NEt₄[FeCl₄], 70 mM Fe, 2 scans (beamline X9B at NSLS, 13 detector elements); NEt₄[FeBr₄], 45 mM Fe, 2 scans (beamline X9B at NSLS, 12 detector elements).

Data Analysis. The treatment of raw EXAFS data to yield $\chi(k)$ is discussed in detail in review articles.^{33,34} Our specific data analysis protocol using the programs EXAFSPAK³⁵ and SSEXafs^{31,36} was previously described.¹⁸ Curve-fitting of XANES data to obtain preedge peak areas included the following: The edge was modeled as an integral of a 75% Gaussian peak and a 25% Lorentzian peak. The heights, positions, and widths (at half-height) of preedge peaks were refined using a Gaussian function. Refinements with multiple peaks were constrained to have a common width for all peaks. Preedge peak areas are in percentage of Fe K-edge height (eV) and were multiplied by 100. EXAFS fitting parameters A (amplitude reduction factor) and ΔE (phase shift) for N/O and C scatterers had been extracted from Fe(acac)₃.³¹ Fitting parameters for Cl and Br scatterers were determined by fitting the EXAFS spectrum of crystallographically characterized NEt₄[FeCl₄] and NEt₄[FeBr₄], respectively. The parameters r and n were fixed to the crystallographically determined values $r_{\text{Fe-Cl}} = 2.185$ Å and $r_{\text{Fe-Br}} = 2.337$ Å, while A and ΔE were refined and the goodness-of-fit (GOF) value was minimized (Supporting Information, Figures S6–S9).

Density Functional Theory (DFT) Calculations. The DFT calculations were performed using Becke's three-parameter hybrid functional (B3LYP) and basis set 6-311G provided by the *Gaussian03* (revision C.02) software package.³⁷ The ⁵⁷Fe hyperfine parameters were calculated using the properties keyword of the Gaussian code. The ⁵⁷Fe isomer shifts, δ , were evaluated from the DFT charge density at the iron nucleus using the calibration given by Vrajmasu et al.³⁸ The self-consistent-field procedures and geometry optimizations were terminated upon reaching the default

convergence criteria. The optimized structures for **2**–X were used for the calculations of the hyperfine parameters listed in Table 1. Final coordinates for **2**–X are listed in Table S7 in the Supporting Information.

Results

I. Formation of $[\text{Fe}^{\text{IV}}(\text{O})(\text{TPA})(\text{NCMe})]^{2+}$ (**2**–NCMe).

The direct formation of **2**–NCMe from $[\text{Fe}^{\text{II}}(\text{TPA})(\text{NCMe})_2]^{2+}$ (**1**–NCMe) has thus far only been observed with stoichiometric AcO₂H as the oxidant, occurring presumably via heterolytic O–O bond cleavage, with full formation requiring low temperatures, e.g., -40 °C.¹² At -40 °C, this intermediate persists for at least 1 day. The sixth ligand is assumed to be acetonitrile because it is the solvent and by precedence of the crystallographically characterized $[\text{Fe}^{\text{IV}}(\text{O})(\text{TMC})(\text{NCMe})]^{2+}$.¹¹ Upon warming to room temperature, metastable **2**–NCMe converts to the oxo-bridged diiron(III) complex $[\text{Fe}^{\text{III}}_2(\mu\text{-O})(\mu\text{-OAc})(\text{TPA})_2]^{3+}$, as indicated by the isosbestic appearance of UV–visible features characteristic of the latter and a Mössbauer analysis of the decayed species.¹² Further evidence for the nature of the decayed species is provided by a structural determination on a dark-green single crystal that was obtained over the course of several days after the addition of diethyl ether to the solution of **2**–NCMe at -40 °C (Supporting Information, Tables S1 and S2 and Figure S1).

The stoichiometric formation of **2**–NCMe from the addition of AcO₂H to **1**–OTf in acetonitrile is remarkable,

(33) Scott, R. A. *Methods Enzymol.* **1985**, *117*, 414–459.

(34) Teo, B.-K.; Joy, D. C. *EXAFS Spectroscopy, Techniques and Applications*; Plenum Press: New York, 1981.

(35) George, G. N.; Pickering, I. J. *EXAFSPAK*; Stanford Synchrotron Radiation Laboratory, Stanford Linear Accelerator Center: Stanford, CA, 2000.

(36) Scarrow, R. C.; Trimitsis, M. G.; Buck, C. P.; Grove, G. N.; Cowling, R. A.; Nelson, M. J. *Biochemistry* **1994**, *33*, 15023–15035.

(37) Frisch, M. J.; Trucks, G. W.; Schlegel, H. B.; Scuseria, G. E.; Robb, M. A.; Cheeseman, J. R.; Montgomery, J. A., Jr.; Vreven, T.; Kudin, K. N.; Burant, J. C.; Millam, J. M.; Iyengar, S. S.; Tomasi, J.; Barone, V.; Mennucci, B.; Cossi, M.; Scalmani, G.; Rega, N.; Petersson, G. A.; Nakatsuji, H.; Hada, M.; Ehara, M.; Toyota, K.; Fukuda, R.; Hasegawa, J.; Ishida, M.; Nakajima, T.; Honda, Y.; Kitao, O.; Nakai, H.; Klene, M.; Li, X.; Knox, J. E.; Hratchian, H. P.; Cross, J. B.; Bakken, V.; Adamo, C.; Jaramillo, J.; Gomperts, R.; Stratmann, R. E.; Yazyev, O.; Austin, A. J.; Cammi, R.; Pomelli, C.; Ochterski, J. W.; Ayala, P. Y.; Morokuma, K.; Voth, G. A.; Salvador, P.; Dannenberg, J. J.; Zakrzewski, V. G.; Dapprich, S.; Daniels, A. D.; Strain, M. C.; Farkas, O.; Malick, D. K.; Rabuck, A. D.; Raghavachari, K.; Foresman, J. B.; Ortiz, J. V.; Cui, Q.; Baboul, A. G.; Clifford, S.; Cioslowski, J.; Stefanov, B. B.; Liu, G.; Liashenko, A.; Piskorz, P.; Komaromi, I.; Martin, R. L.; Fox, D. J.; Keith, T.; Al-Laham, M. A.; Peng, C. Y.; Nanayakkara, A.; Challacombe, M.; Gill, P. M. W.; Johnson, B.; Chen, W.; Wong, M. W.; Gonzalez, C.; Pople, J. A. *Gaussian 03*, revision C.02; Gaussian, Inc.: Wallingford, CT, 2004.

(38) Vrajmasu, V.; Münck, E.; Bominaar, E. L. *Inorg. Chem.* **2003**, *42*, 5974–5988.

and the solvent is a key factor in this transformation. When the same reaction was carried out in dichloromethane, an oxoiron(IV) species was not observed to form at all; instead, full conversion to $[\text{Fe}^{\text{III}}_2(\mu\text{-O})(\mu\text{-OAc})(\text{TPA})_2]^{3+}$ was obtained with 0.5 equiv of peracid, even at -80°C . This is not an unexpected outcome for the oxidation of iron(II) complexes because $(\mu\text{-oxo})$ diiron(III) complexes are usually considered the thermodynamic sink in such reactions.³⁹ It is likely that an $\text{Fe}^{\text{IV}}=\text{O}$ complex does form in CH_2Cl_2 , but it reacts readily with its precursor to form a $(\mu\text{-oxo})$ diiron(III) complex. In contrast, **1**-NCMe could be titrated in MeCN solution with substoichiometric amounts of AcO_2H to afford **2**-NCMe, achieving full formation at 1 equiv of peracid. It would thus appear that there is a kinetic barrier to the reaction of **2**-NCMe with its precursor that allows the oxoiron(IV) complex to be observed and persist in MeCN solution at -40°C . We suggest that this barrier arises from the low-spin nature ($S = 0$) of **1**-NCMe, which makes it kinetically inert. On the other hand, **1**-OTf remains high-spin ($S = 2$) and kinetically labile in CH_2Cl_2 and can thus react rapidly with **2**-OTf that presumably forms upon the addition of AcO_2H . In addition, the presumed coordination of MeCN stabilizes the oxoiron(IV) center and extends its lifetime (see below), so the use of MeCN as a solvent played a crucial role in the discovery of this family of oxoiron(IV) complexes.

II. Ligand Substitution at 2-NCMe. A. Generation of $[\text{Fe}^{\text{IV}}(\text{O})(\text{TPA})(\text{X})]^{2+}$, $\text{X} = \text{OC}(\text{O})\text{CF}_3$ (2**- O_2CCF_3), Cl (**2**- Cl), and Br (**2**- Br).** The addition of 3 equiv of $\text{NEt}_4\text{CF}_3\text{CO}_2$ to **2**-NCMe in acetonitrile at -40°C results in an immediate shift of its characteristic near-IR absorption maximum from 724 to 745 nm, indicating the formation of a new species designated as **2**- O_2CCF_3 (Figure 1, top). Direct evidence for the coordination of trifluoroacetate to the metal center is provided by ^{19}F NMR spectroscopy. In CD_3CN , **2**-NCMe (i.e., **2**- NCCD_3) exhibits a ^{19}F NMR resonance at -80 ppm (-35°C), which can be attributed to free triflate counterions. The addition of 1 equiv of $\text{NEt}_4\text{CF}_3\text{CO}_2$ to this solution results in the appearance of resonances near -76 ppm and at -84 ppm (Figure S2B in the Supporting Information; see the Experimental Section and Figure S2A in the Supporting Information for ^{19}F NMR spectroscopic data of **1**- O_2CCF_3). The peak at -84 ppm is assigned to CF_3CO_2^- ligated to the paramagnetic iron(IV) center, while the peak close to -76 ppm corresponds to free CF_3CO_2^- . In support, the addition of another 1 equiv of $\text{NEt}_4\text{CF}_3\text{CO}_2$ results in an increased intensity of the latter peak. Moreover, the intensity of the ^{19}F NMR resonance assigned to **2**- O_2CCF_3 decreases when the sample is warmed to room temperature, consistent with the expected decay of metastable **2**- O_2CCF_3 . Thus, trifluoroacetate can displace the solvent ligand in **2**-NCMe to form **2**- O_2CCF_3 . For comparison, the ^{19}F NMR resonance of **2**- O_2CCF_3 is upfield shifted by ~ 8 ppm with respect to that of $[\text{Fe}^{\text{IV}}(\text{O})(\text{TMC})(\text{OC}(\text{O})\text{CF}_3)]^{2+}$,²⁶ presumably because of different properties of the paramagnetic iron(IV) centers and the cis versus trans stereochemistry with respect to the oxo ligand.

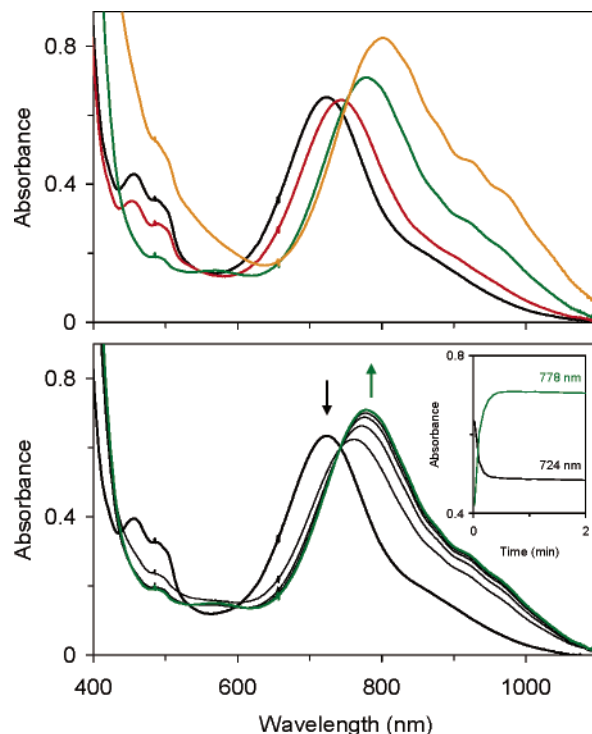
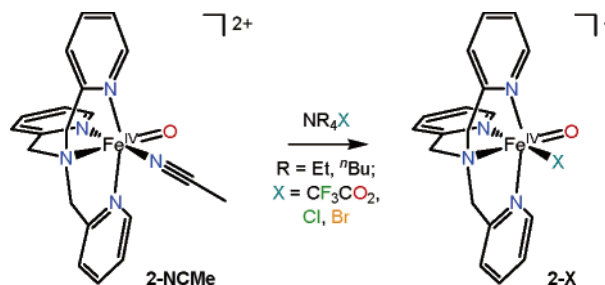


Figure 1. Top: Electronic absorption spectra of 2 mM $[\text{Fe}^{\text{IV}}(\text{O})(\text{TPA})(\text{NCMe})]^{2+}$, **2**-NCMe (—, black), $[\text{Fe}^{\text{IV}}(\text{O})(\text{TPA})\{\text{OC}(\text{O})\text{CF}_3\}]^{2+}$, **2**- O_2CCF_3 (—, red), $[\text{Fe}^{\text{IV}}(\text{O})(\text{TPA})(\text{Cl})]^{2+}$, **2**-Cl (—, green), and $[\text{Fe}^{\text{IV}}(\text{O})(\text{TPA})(\text{Br})]^{2+}$, **2**-Br (—, yellow) in MeCN (1-cm cuvette). Bottom: Conversion of 2 mM **2**-NCMe (—, black) to **2**-Cl (—, green) in MeCN at -40°C by the addition of 3 equiv of NBu_4Cl . Inset: Corresponding time course of the reaction monitored at 724 and 778 nm.

Scheme 1. Ligand Substitution Reactions of Oxoiron(IV) Complex **2**-NCMe



Similarly, treatment of **2**-NCMe with 3 equiv of NBu_4Cl or NBu_4Br at -40°C affords the new species **2**-Cl or **2**-Br over a 20-s time period. These complexes have absorption maximum wavelengths of 778 and 800 nm, respectively, with higher extinctions than the parent complex ($\epsilon = 350 \text{ M}^{-1}\cdot\text{cm}^{-1}$ for **2**-Cl and $400 \text{ M}^{-1}\cdot\text{cm}^{-1}$ for **2**-Br; Figure 1, top, and Scheme 1). The observation of an isosbestic point in the course of reaction between **2**-NCMe and NBu_4Cl suggests that **2**-Cl is directly produced from **2**-NCMe (Figure 1, bottom). New features also appear in the visible region after formation of **2**-Cl and **2**-Br; the chromophore at 460 nm attributed to the $[\text{Fe}^{\text{III}}_2(\mu\text{-O})(\mu\text{-OAc})(\text{TPA})_2]^{3+}$ byproduct is not observed and is replaced by absorption shoulders at 490 nm, consistent with the formation of $[\text{Fe}^{\text{III}}_2(\mu\text{-O})(\text{TPA})_2(\text{Cl})_2]^{2+}$ and $[\text{Fe}^{\text{III}}_2(\mu\text{-O})(\text{TPA})_2(\text{Br})_2]^{2+}$ as byproducts.^{40,41}

(39) Kurtz, D. M., Jr. *Chem. Rev.* **1990**, *90*, 585–606.

Unlike the substitution reactions with CF_3CO_2^- , Cl^- , and Br^- , the reaction of **2**-NCMe with I^- leads to the immediate decay of the oxoiron(IV) complex, as indicated by the disappearance of the near-IR chromophore associated with **2**. Also, the addition of 3 equiv of fluoride or acetate promotes decay of **2**-NCMe ($t_{1/2}$ at -40°C is ca. 10 min upon the addition of 3 equiv of fluoride and ca. 30 s upon the addition of 3 equiv of acetate). In these cases, a shift of the absorption maximum wavelength from 724 nm to approximately 735–745 nm can be discerned during decay. Addition of a larger excess of fluoride or acetate ions only accelerated the decay.

It would thus appear that various monoanionic ligands can be introduced at the sixth coordination site of **2**, and these ligand substitutions can alter the stability of the oxoiron(IV) unit. For example, while **2**-NCMe and **2**- O_2CCF_3 are stable at -40°C for hours, **2**-Cl and **2**-Br decay with half-lives of ca. 4 and 2 h, respectively. When solutions of **2**-X are warmed to 10°C , their lifetimes can qualitatively be described as decreasing in the order **2**-NCMe > **2**- O_2CCF_3 > **2**-Cl \sim **2**-Br. The observed rapid decay of **2**-NCMe in the presence of added acetate further supports the assignment of acetonitrile as the sixth ligand in **2** derived from the reaction of **1**-NCMe with AcO_2H rather than the acetate or acetic acid byproduct.

It is noteworthy that **2**-Cl and **2**-Br can only be generated by ligand exchange at **2**-NCMe. Attempts to generate **2**-X by the oxidation of $[\text{Fe}^{\text{II}}(\text{TPA})(\text{X})(\text{NCMe})]^+$, X = Cl (**1**-Cl) or Br (**1**-Br), with AcO_2H were not successful; however, a small amount of **2**- O_2CCF_3 can be formed from **1**- O_2CCF_3 , together with an oxo-bridged diiron(III) complex (under the conditions used for **2**-NCMe: in MeCN, -40°C , 1 equiv of AcO_2H). These differences support our proposal that the low-spin nature of **1**-NCMe (vs high-spin for the **1**-X complexes) is an important factor in the trapping of **2**-NCMe.

B. Ligand-Field Considerations. The observed shifts of the near-IR chromophores of **2**-NCMe, **2**- O_2CCF_3 , **2**-Cl, and **2**-Br can be rationalized by consideration of the relative ligand-field strengths of the sixth ligands (Table 1). By analogy to an MCD spectroscopic study of $[\text{Fe}^{\text{IV}}(\text{O})(\text{TMC})(\text{NCMe})]^{2+}$ in combination with DFT calculations,²⁰ the features in the 720–800-nm range are proposed to arise from three ligand-field transitions: $3d_{xz/yz} \rightarrow 3d_{x^2-y^2}$, $3d_{xy} \rightarrow 3d_{x^2-y^2}$ (equatorial ligand-field strength), and $3d_{xy} \rightarrow 3d_{xz/yz}$ (Fe–O π bond strength), with the z axis being defined by the Fe–O bond. Substitution in the xy plane of an oxoiron(IV) complex should modulate the equatorial ligand field and thus mainly affect the energy of the antibonding $3d_{x^2-y^2}$ orbital, so the $3d_{xz/yz} \rightarrow 3d_{x^2-y^2}$ and $3d_{xy} \rightarrow 3d_{x^2-y^2}$ transitions should then red-shift with a weaker-field ligand according to the spectrochemical series, while the $3d_{xy} \rightarrow 3d_{xz/yz}$ transition should be affected to a lesser extent. Indeed the near-IR chromophores of the **2**-X complexes order in energy according

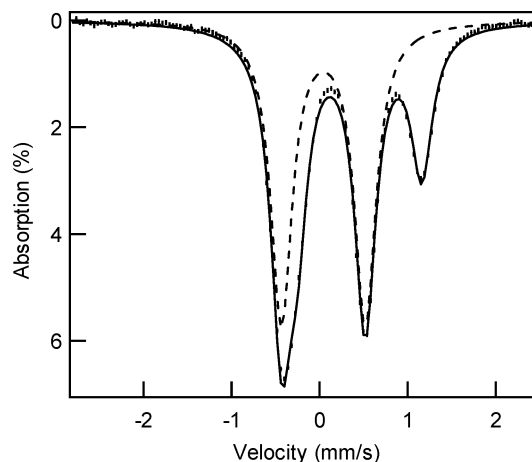


Figure 2. Zero-field Mössbauer spectrum of **2**-Cl in acetonitrile recorded at 4.2 K. The solid line is a least-squares fit to two quadrupole doublets representing the contributions of **2**-Cl (68% of the total Fe) and a (μ -oxo)diiron(III) species. The dashed line gives the contribution of **2**-Cl. Spectra of the other complexes discussed in the text are shown in Figure S3 in the Supporting Information.

to the positions of the X ligands in the spectrochemical series $\text{MeCN} > \text{CF}_3\text{CO}_2^- > \text{Cl}^- > \text{Br}^-$, supporting the assignment of the bands in the 720–800-nm region to d–d transitions.

III. Mössbauer Spectra. The equatorial-ligand-substituted oxoiron(IV) complexes **2**- O_2CCF_3 , **2**-Cl, and **2**-Br were further characterized by Mössbauer spectroscopy to ascertain their iron oxidation and spin-state assignments and to investigate how variation of the sixth ligand influences the Mössbauer parameters of the oxoiron(IV) center. The zero-field Mössbauer spectra of ^{57}Fe -enriched samples of **2**- O_2CCF_3 , **2**-Cl, and **2**-Br in a frozen acetonitrile solution consist of doublets with isomer shifts δ of 0.02, 0.04, and $0.06 \text{ mm}\cdot\text{s}^{-1}$, respectively, and very similar quadrupole splittings ΔE_Q of around $0.95 \text{ mm}\cdot\text{s}^{-1}$ (Figures 2 and S3 in the Supporting Information). These doublets account for 75% of the ^{57}Fe in **2**- O_2CCF_3 , 68% in **2**-Cl, and 61% in **2**-Br. The balance of the ^{57}Fe present can be ascribed to a doublet arising from diamagnetic (μ -oxo)diiron(III) byproducts ($\delta = 0.45 \text{ mm}\cdot\text{s}^{-1}$; $\Delta E_Q \sim 1.45 \text{ mm}\cdot\text{s}^{-1}$) and in the case of **2**-Br approximately 10% high-spin iron(III) monomer. Although the low-energy lines of the oxoiron(IV) and (μ -oxo)diiron(III) doublets overlap, their parameters can be determined with good accuracy by comparing preparations with different ratios of the two species. By matching of the intensities of the resolved high-energy lines of the oxoiron(IV) doublet and subtraction of the spectra, a good spectral representation of (μ -oxo)diiron(III) species could be obtained. As a representative example, we show in Figure 2 the spectrum obtained for a **2**-Cl sample.

IV. XAS of **2**-X, X = NCMe, $\text{OC}(\text{O})\text{CF}_3$, Cl, and Br.

A. X-ray Absorption Near-Edge Structures. XAS data at the Fe K edge were measured for the intermediates **2**- O_2CCF_3 , **2**-Cl, and **2**-Br. The near-edge structures are shown in Figure 3. The Fe K edges for halide-substituted **2**-Cl and **2**-Br are downshifted by ca. 1 eV relative to those of **2**-NCMe^{12,18} and **2**- O_2CCF_3 but retain a similar shape. The larger iron(III) fractions in these samples could be responsible for the lower edge energy. However, two samples of **2**-Cl

(40) Norman, R. E.; Holz, R. C.; Ménage, S.; O'Connor, C. J.; Zhang, J. H.; Que, J., L. *Inorg. Chem.* **1990**, *29*, 4629–4637.

(41) Kojima, T.; Leising, R. A.; Yan, S.; Que, L., Jr. *J. Am. Chem. Soc.* **1993**, *115*, 11328–11335.

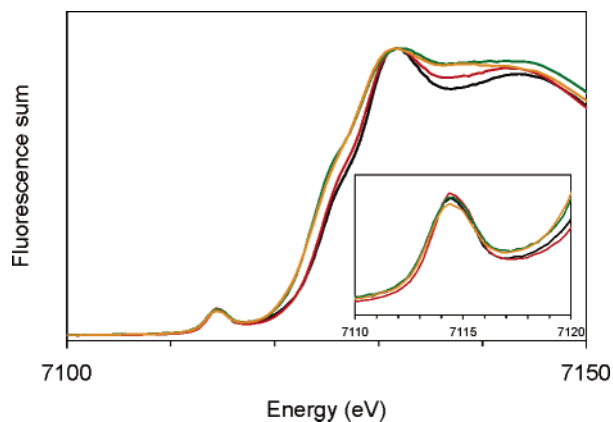


Figure 3. Fe K-edge X-ray absorption near-edge structures (XANES; fluorescence excitation) of **2**-NCMe (—, black), **2**-O₂CCF₃ (—, red), **2**-Cl (—, green), and **2**-Br (—, yellow).

with different ratios of Fe^{IV}/Fe^{III} of 68:32 and 51:49 were found to have the same edge energy. Therefore, the downshift may rather be attributed to the coordination of the halide ligand. As for the parent **2**-NCMe, the preedge regions of substituted **2**-O₂CCF₃, **2**-Cl, and **2**-Br display peaks at 7114.5 eV with similar intensities for all three complexes (24–27 units; Table 1). These peaks are assigned to 1s → 3d transitions. We have previously reported such intense features (24.5–29.3 units) in the range of 7114.1–7114.6 eV for other *S* = 1 oxoiron(IV) complexes.¹⁸ The energies observed for **2**-O₂CCF₃, **2**-Cl, and **2**-Br are thus consistent with the iron(IV) oxidation state. The high intensity arises from significant mixing of 3d and 4p orbitals due to strong Fe=O π bonding that leads to a large deviation from centrosymmetry of the iron ligand field.

B. EXAFS Spectra and Fitting Results. The Fourier transforms (*r'* space) of the Fe K-edge EXAFS data of the [Fe^{IV}(O)(TPA)(X)]^{2+/+} series **2**-NCMe, **2**-O₂CCF₃, **2**-Cl, and **2**-Br are shown in Figure 4, and selected fitting results are compared in Table 2. The fitting protocol used for all three anion-bound complexes follows the procedure that we have used for **2**-NCMe, and a complete list of fits for each complex can be found in the Supporting Information (Table S4). The spectrum of **2**-NCMe exhibits a prominent feature centered at *r'* = 1.5 Å, where *r'* corresponds to the actual metal–scatterer distance *r* after a phase shift correction of approximately 0.4 Å (*r* ≈ *r'* + 0.4 Å). This peak arises from the first coordination sphere of the *S* = 1 iron(IV) center. As previously reported, the EXAFS spectrum of **2**-NCMe can be best described by three shells of absorber–scatterer interactions: one oxygen/nitrogen scatterer at an Fe–N/O distance (*r*) of 1.65 Å, four nitrogen/oxygen scatterers at 1.98 Å, and six carbon scatterers at 2.89 Å, accounting for the oxo ligand and the nitrogen donor and carbon backbone atoms of the TPA ligand, respectively.¹⁸ Substitution of the labile solvent ligand in **2**-NCMe by trifluoroacetate affording **2**-O₂CCF₃ results in only minor changes in the EXAFS spectrum (Figure 4A), as might be expected for an nitrogen/oxygen atom exchange in the iron coordination sphere. While a similar three-shell fit can be obtained for **2**-O₂CCF₃ (Table 2, fit 3), introduction of an additional Fe–N/O shell at 2.19 Å further improves the fit (Table 2, fit 1, and Figure 4B),

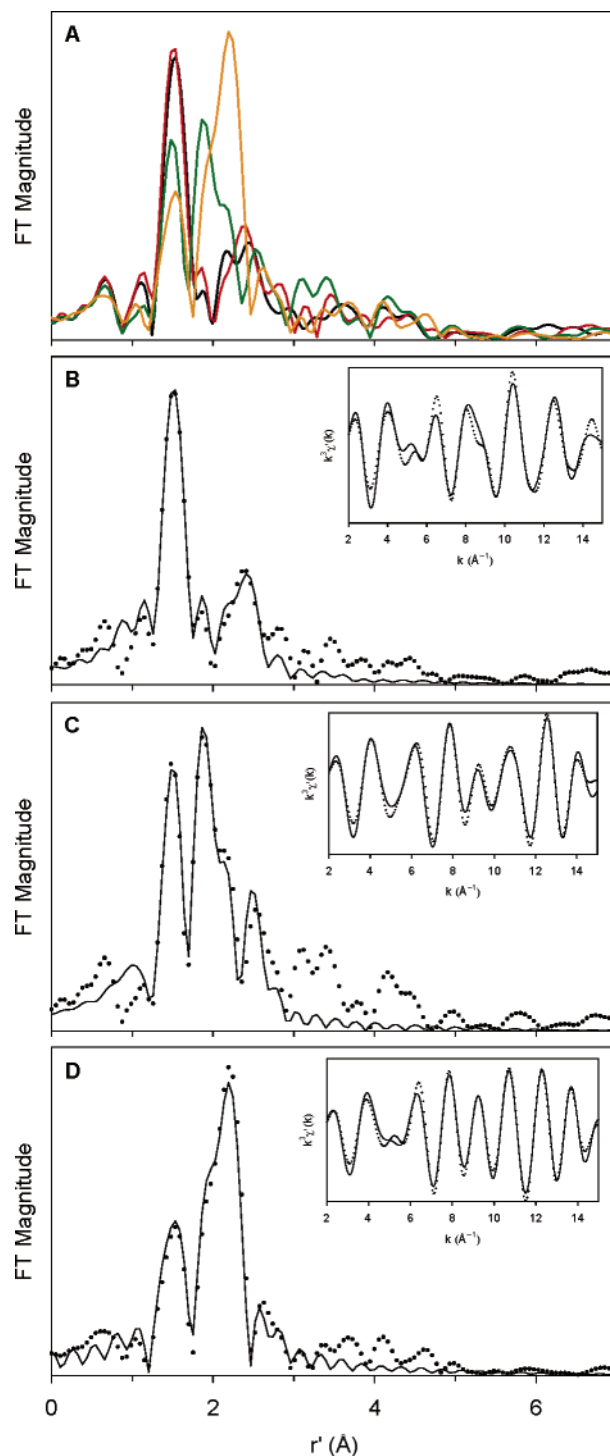


Figure 4. (A) Fourier transforms of the Fe K-edge EXAFS data [$k^3\chi(k)$] of **2**-NCMe (—, black), **2**-O₂CCF₃ (—, red), **2**-Cl (—, green), and **2**-Br (—, yellow). Fourier transforms of the Fe K-edge EXAFS data [$k^3\chi(k)$] and Fourier-filtered EXAFS spectra [$k^3\chi'(k)$, insets] of (B) **2**-O₂CCF₃ [Fourier-transformed range $k = 2$ – 15 \AA^{-1} with experimental data (···) and fit 1 O/N, 4 N/O, 1 N/O, 6 C (—) and back-transformation range $r' = 0.70$ – 3.30 \AA], (C) **2**-Cl [Fourier-transformed range $k = 2$ – 15 \AA^{-1} with experimental data (···) and fit 1 O/N, 3 N/O, 1 N/O, 1 Cl, 4 C (—) and back-transformation range $r' = 0.75$ – 2.95 \AA], and (D) **2**-Br [Fourier-transformed range $k = 2$ – 15 \AA^{-1} with experimental data (···) and fit 0.7 O/N, 3 N/O, 1.5 N/O, 1 Br, 4 C (—) and back-transformation range $r' = 0.75$ – 3.25 \AA].

which could be attributed to the Fe–N distance in the minor high-spin (μ -oxo)diiron(III) decay product. (This distance

Table 2. EXAFS Fitting Results for **2**–NCMe, **2**–O₂CCF₃, **2**–Cl, and **2**–Br^a

complex	fit	Fe–O/N			Fe–N/O			Fe–N/O			Fe–X (X = Cl or Br)			Fe···C			GOF $\epsilon^2 \times 10^3$ ^b
		<i>n</i>	<i>r</i> (Å)	$\Delta\sigma^2$	<i>n</i>	<i>r</i> (Å)	$\Delta\sigma^2$	<i>n</i>	<i>r</i> (Å)	$\Delta\sigma^2$	<i>n</i>	<i>r</i> (Å)	$\Delta\sigma^2$	<i>n</i>	<i>r</i> (Å)	$\Delta\sigma^2$	
2 –NCMe ^c	1	1	1.65	0.3	4	1.98	2.4							6	2.89	3.8	
2 –O ₂ CCF ₃	1	1	1.66	–1.3	4	1.98	2.5	1	2.19	2				6	2.90	3.5	0.863
	(1	1	1.66	–0.9	4	1.98	2.2	1	2.18	0.5				6	2.90	4.0	0.99) ^d
	2	1	1.66	–1.2	4	1.98	2.5	1	2.19	1							1.25
	3	1	1.66	–1.4	4	1.98	3.0							6	2.90	3.2	0.94
2 –Cl	4				4	1.98	1.4	1	2.15	–1.6				6	2.90	4	1.67
	1	1	1.65	1.0	3	1.98	4.8	1	2.16	1	1	2.29	–0.7	4	2.92	1.9	0.718
	(1	1	1.66	1.2	3	1.98	3.9	1	2.14	–1.8	1	2.30	–0.4	4	2.93	0.7	1.01) ^d
	(1	0.8	1.65	–0.4	3	1.99	6	1	2.17	4	1	2.29	–1.0	4	2.92	2.0	0.654) ^e
	2	1	1.65	1.2	3	1.99	5	1	2.18	2	1	2.28	–0.8				1.07
	3	1	1.65	0.5	3	2.00	7.2				1	2.29	–1.3	4	2.92	2.3	0.72
2 –Cl/ ^f 2 –Br	4				2	1.97	0.9	2	2.17	3	1	2.28	–0.1	4	2.92	2	1.19
		0.6	1.66	0.4	2	1.95	6	2	2.13	2.2	1	2.30	–0.5	4	2.93	4.0	
	1	0.7	1.66	1.8	3	1.98	3.7	1.5	2.16	0.2	1	2.43	0	4	2.92	3.5	0.720
	(1	0.7	1.65	2.9	3	1.99	3.1	1.5	2.17	–0.9	1	2.43	0.1	4	2.92	3.9	0.85) ^d
	2	0.7	1.66	1.9	3	1.99	3.9	1.5	2.17	0.3	1	2.43	0.1				1.06
	3	0.7	1.66	0.2	3	2.02	9				1	2.43	–0.1	4	2.91	3.4	0.84
	4				3	1.99	3.7	1.5	2.17	–0.5	1	2.43	0.1	4	2.92	4	1.04

^a Fourier-transformed range for **2**–NCMe, **2**–O₂CCF₃, **2**–Cl, and **2**–Br: $k = 2$ –15 Å^{–1} (resolution 0.12 Å). r is in units Å and $\Delta\sigma^2$ in 10³ Å². The typical error of analysis for interatomic distances (r) is approximately ± 0.02 Å.³³ ^b Back-transformation ranges are as follows: for **2**–O₂CCF₃, $r' = 0.70$ –3.30 Å; for **2**–Cl, $r' = 0.75$ –2.95 Å; for **2**–Br, $r' = 0.75$ –3.25 Å. ^c From ref 18. ^d Fits to unfiltered data corresponding to the best fits to filtered data. ^e The short-distance Fe–O/N shell associated with the oxo ligand could also be refined with an occupancy of $n < 1$. ^f Second independent sample of **2**–Cl (see the Supporting Information, Figure S5 and Table S4).

also had been observed for a second independent sample of **2**–NCMe.^{12,18)}

In contrast to **2**–NCMe and **2**–O₂CCF₃, the r' space spectra of **2**–Cl and **2**–Br exhibit additional intense peaks at $r' = 1.9$ and 2.2 Å, respectively, that can only be attributed to a high- Z scatterer that is coordinated to iron (Figure 4A). In fact, this latter feature becomes dominant in the spectrum of **2**–Br. Fits to the EXAFS spectra of **2**–Cl and **2**–Br reveal low- Z shells at 1.66 and 1.98 Å, as for **2**–NCMe and **2**–O₂CCF₃, but require one additional shell with a chlorine scatterer at 2.29 Å for **2**–Cl and a bromine scatterer at 2.43 Å for **2**–Br (Table 2). These scatterers account for the additional intense peaks in the Fourier-transformed EXAFS spectra and provide evidence for the substitution of one ligand in **2**–NCMe as suggested by the optical spectra (compare section II.A and Figure 1). Another Fe–N/O shell can be refined to a distance at ca. 2.15 Å. While the inclusion of this subshell does not necessarily improve the global fit (see the GOF value), it leads to a lower Debye–Waller factor for the 2.0-Å shell, indicating considerable disorder in the Fe–N_{TPA} distances. This subshell may be attributed to the Fe–N distance of the high-spin diiron(III) byproducts, which were found to make up $\sim 30\%$ of the iron in the samples by Mössbauer analysis.

The best fits to the Fourier-filtered EXAFS spectra [$k^3\chi'(k)$] of **2**–Cl and **2**–Br require coordination numbers of 1 for both chlorine and bromine scatterers and small Debye–Waller factors, despite the fact that the oxoiron(IV) centers make up only $\sim 70\%$ of the samples (Table 2 and Figure 4, panels C and D). This observation suggests that the halide is ligated to the iron center in both the low-spin iron(IV) and the high-spin iron(III) components of these samples. The small Debye–Waller factors indicate little disorder in the Fe–Cl and Fe–Br shells of **2**–Cl and **2**–Br samples, implying very similar Fe^{IV}–X and Fe^{III}–X distances. The assignment of the 2.29-Å shell to the Fe–Cl distances in

both [Fe^{IV}(O)(TPA)(Cl)]⁺ and its decomposition product is further corroborated by the EXAFS analysis of the two samples of different percentages of **2**–Cl (68 and 51%), which reveals similar parameters for the Fe–Cl shell (Table 2 and Figure S5). The diiron(III) byproduct in the **2**–Cl samples is very likely [Fe^{III}₂(μ-O)(TPA)₂(Cl)₂]²⁺, which has an Fe–Cl distance of ~ 2.31 Å (i.e., 2.298, 2.303, and 2.319 Å)^{41,43} that matches well with the Fe–Cl distance in samples of **2**–Cl.

V. DFT Calculations. In support of the accumulated experimental data, we carried out DFT calculations to obtain geometry-optimized structures for **2**–NCMe, **2**–O₂CCF₃, **2**–Cl (Figure 5), and **2**–Br (see Table S7 in the Supporting Information for calculated coordinates). Metal–ligand distances obtained from these calculations have been listed in square brackets in Table 1 and are in good agreement with the experimental data.

Table 1 also lists calculated Mössbauer parameters. As noted from the experimental results, the parameters δ and ΔE_Q are rather insensitive to the nature of the exchangeable equatorial ligand in the [Fe^{IV}(O)(TPA)(X)]^{2+/+} series. The calculated values are in good agreement with the experimental data and exhibit only a marginally greater variance in the quadrupole splitting ($\Delta E_Q = 0.86$ –1.23 mm·s^{–1} calcd vs 0.92–0.95 mm·s^{–1} exptl).⁴⁴ The insensitivity of the hyperfine parameters to substitution of X indicates that the net electronic charge donation from the ligands to the metal is approximately constant throughout the series. In all cases,

(42) Randall, C. R.; Shu, L.; Chiou, Y.-M.; Hagen, K. S.; Ito, M.; Kitajima, N.; Lachicotte, R. J.; Zang, Y.; Que, L., Jr. *Inorg. Chem.* **1995**, *34*, 1036–1039.

(43) Hazell, A.; Jensen, K. B.; McKenzie, C. J.; Toftlund, H. *Inorg. Chem.* **1994**, *33*, 3127–3134.

(44) The calculated δ values are 0.03–0.06 mm·s^{–1} too large, which is almost within the expected uncertainty. For reasons not yet fully understood, the calculated isomer shifts for the Fe(O)TMC complexes match the experimental data better than those calculated for complexes with pyridine ligands.

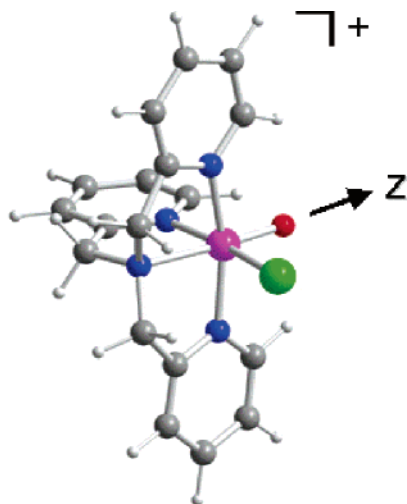


Figure 5. Geometry-optimized DFT structure of **2-Cl** obtained with *Gaussian03*, using the functional/basis set B3LYP/6-311G. Color key: pink, iron; blue, nitrogen; gray, carbon; red, oxygen; green, chlorine.

Table 3. Orbital Populations of d Orbitals and ΔE_Q Values

	orbital population ^a					ΔE_Q (mm·s ⁻¹)		
	xy	xz	yz	$x^2 - y^2$	z^2	est. ^b	DFT	exp.
2-NCMe	1.915	1.456	1.399	0.585	0.823	1.02	0.86	0.93
2-O₂CCF₃	1.917	1.423	1.408	0.578	0.828	1.00	1.12	0.92
2-Cl	1.921	1.417	1.394	0.639	0.838	1.27	1.22	0.95
2-Br	1.918	1.419	1.385	0.656	0.839	1.34	1.23	0.95

^a The z axis is along the Fe=O bond, and the x axis is along Fe-X.

^b Quadrupole splitting estimated with the simple expression $\Delta E_Q(\text{est.}) = \sum_d P(d) V_{zz}(d)$, where $V_{zz}(d) = -4$ (d = z^2), 4 ($x^2 - y^2$), 4 (xy), -2 (xz), -2 (yz) mm·s⁻¹ and P(d) is the population of orbital d.

the vacant 3d orbitals [i.e., $(xz)^\beta$, $(yz)^\beta$, $(z^2)^{\alpha\beta}$, and $(x^2 - y^2)^{\alpha\beta}$] for the ground state $S = 1$ configuration $|(xy)^2(xz)^\alpha(yz)^\alpha|$ accept electronic charges from both the axial ligands $\{(xz)^\beta$, $(yz)^\beta$, $(z^2)^{\alpha\beta}\}$ and the equatorial ligands. (The predominant acceptor orbital is $(x^2 - y^2)^{\alpha\beta}$, which has σ interactions with both the TPA and the exchangeable ligand; the orbitals $(xz)^\beta$ and $(yz)^\beta$ accept less charge because they are engaged in π interactions.) Because the oxo ligand is by far the strongest donor in the coordination sphere and the ligand substitution involves only one out of the four weaker equatorial donors, it is not surprising that the changes in the orbital populations (shown in Table 3) and the corresponding differences in the hyperfine parameters of iron are minor. (In contrast, exchange of a ligand trans to the oxo group, as in the Fe(O)(TMC)(X) series, has a much stronger effect on these parameters.²⁷) Moreover, when the weakly π -acidic MeCN ligand in **2-NCMe** is exchanged with a more basic anionic ligand, the TPA ligand responds by donating less charge to iron, thereby offsetting, in part, the electron donation to the $x^2 - y^2$ orbital. As expected, the Mulliken population most affected by the ligand substitution is that of the $x^2 - y^2$ orbital (Table 3). However, the changes are only marginal (<0.08 throughout the series) and correspond to differences of <0.34 mm·s⁻¹ in ΔE_Q (based on the relationship of 4.0 mm·s⁻¹ per electron; compare the third column from the right of Table 3); the variance, though small, is larger than that observed experimentally. The population of the $x^2 - y^2$ orbital and the DFT value for ΔE_Q (second column from

Table 4. Ligand-Substitution-Induced Shifts (cm⁻¹) of Calculated Excitation Energies for **2-X** Relative to the Energy of the Corresponding Transition for **2-MeCN**^a

	2-O₂CCF₃	2-Cl	2-Br
$xy \rightarrow x^2 - y^2$ ^b	800 ^c	1826	2591
$xy \rightarrow xz/yz$	-2	720	524
	825	1150	1775
$xz/yz \rightarrow x^2 - y^2$	779	1185	1457
	1575	1514	1790
experimental	380	950	1300

^a The transition energies used for evaluating the shifts were calculated as differences of the energies of the 3d-like molecular orbitals involved in the transition. The orbital energies were obtained with the nonhybrid functional SVWN using the B3LYP/6-311G optimized structures. ^b 3d transitions from the ground configuration $|(xy)^2(xz)^\alpha(yz)^\alpha|$. ^c By convention, a positive shift corresponds here to a smaller transition energy.

the right of Table 3) increase consistently in passing from π acidic (MeCN) to basic (Cl⁻ and Br⁻) ligands. The greater variance in the calculated values for ΔE_Q may signal that the electronic relaxation in the Fe-N_{TPA} bonds, which buffers the effect of the ligand substitution on ΔE_Q , is slightly underestimated in the calculations.

The ligand substitutions can be monitored more effectively by focusing on the energies of the 3d excitations that involve the affected orbitals, notably $x^2 - y^2$. The composite band near 800 nm in Figure 1 is also present in the related complex [Fe^{IV}(O)(TMC)(NCMe)]²⁺ and has been assigned by Decker et al. to the transitions $xy \rightarrow x^2 - y^2$, $xz/yz \rightarrow x^2 - y^2$, and $xy \rightarrow xz/yz$.²⁰ The experimental absorption maximum shifts from 724 nm (13 800 cm⁻¹) to 800 nm (12 500 cm⁻¹) in the series **2-NCMe**, **2-O₂CCF₃**, **2-Cl**, and **2-Br**. This trend is in agreement with the changes in the energies for the 3d excitations underlying the ~800-nm band obtained from DFT calculations (Table 4).⁴⁵ Apart from one quasi-degenerate pair of transitions, the transition energies decrease in the order of **2-NCMe**, **2-O₂CCF₃**, **2-Cl**, and **2-Br** (Table 4).

Discussion

The MeCN ligand of **2-NCMe** can be readily replaced by CF₃CO₂⁻, Cl⁻, and Br⁻ in ligand-exchange reactions that lead to the formation of the metastable complexes **2-O₂CCF₃**, **2-Cl**, and **2-Br** (Scheme 1 and Figure 1). Direct evidence for ligand substitution has been obtained by the observation of the ¹⁹F NMR resonance of the bound CF₃-CO₂ group of **2-O₂CCF₃** and of the halide scatterers in the EXAFS analyses of **2-Cl** and **2-Br**. These conversions proceed on a time scale of seconds at -40 °C, as monitored by electronic absorption spectroscopy, and are thus much faster than the exchange reaction of [Fe^{IV}(O)(TMC)(NCMe)]²⁺ with 10 equiv of CF₃CO₂⁻, which proceeds on a time scale of minutes at -20 °C.²⁶ While different electronic factors may affect the rate of ligand exchange at a site trans to an oxo group versus one that is cis, it would

(45) The excitation energies obtained by time-dependent DFT are somewhat larger than those observed. In comparison to the calculations for the TMC complex, we find that our excitation energies are systematically higher than the orbital energies (and corresponding transitions) calculated, with a different functional, by Solomon and co-workers.²⁰ Evaluation of the excitation energies and extinction coefficients is probably best assessed in conjunction with an analysis of the more resolved MCD spectra.

appear likely in this comparison that the greater accessibility of the site of substitution in **2**-NCMe may also be a major factor that controls the rate of exchange. In the case of $[\text{Fe}^{\text{IV}}(\text{O})(\text{TMC})(\text{NCMe})]^{2+}$, it is clear from an examination of its crystal structure that the four methyl substituents of the TMC ligand surrounding the axial MeCN significantly reduce access to this site as compared to **2**-NCMe.¹¹

The **2**-X complexes described here represent a homologous series of oxoiron(IV) complexes, allowing the influence of the equatorial ligand field on the properties of the $S = 1$ oxoiron(IV) unit to be investigated. EXAFS analyses of each of these complexes all require a one-atom low-Z shell at 1.65 Å, confirming the presence of the Fe=O unit. The Fe=O and Fe-N_{TPA} distances within the **2**-X series do not appear to be affected by the nature of the X ligand (Table 2). EXAFS analysis also shows the presence of halide ligands in **2**-Cl and **2**-Br with Fe^{IV}-Cl and Fe^{IV}-Br distances of 2.29 and 2.43 Å, respectively. These distances are shorter than those found for the corresponding Fe^{II}-X distances, 2.31–2.47 Å for X = Cl^{46–51} and 2.48–2.67 Å for X = Br;^{49,52,53} however, they are within the range found for corresponding Fe^{III}-X distances, 2.24–2.34 Å for X = Cl^{41,43,54–56} and 2.38–2.45 Å for X = Br.^{56,57} The latter comparison suggests that the strong covalent bonding to the oxo group absorbs most of the incremental charge on the iron center on going from the 3+ to 4+ oxidation state.^{16,58–60}

Complexes **2**-X exhibit electronic absorption spectra with distinct bands in the 700–800-nm region that can be assigned to ligand-field transitions of the $S = 1$ oxoiron(IV) center.²⁰ The transition energies decrease in the order of **2**-NCMe > **2**-O₂CCF₃ > **2**-Cl > **2**-Br, in agreement with the spectrochemical series (Figure 1 and Table 1). Because variations in the equatorial ligand field would be expected

to affect primarily the energy of the $3d_{x^2-y^2}$ orbital, the downshifted bands may be attributed to the $3d_{xz/yz} \rightarrow 3d_{x^2-y^2}$ and $3d_{xy} \rightarrow 3d_{x^2-y^2}$ transitions, two of the three d-d transitions previously identified from an analysis of the MCD spectrum of $[\text{Fe}^{\text{IV}}(\text{O})(\text{TMC})(\text{NCMe})]^{2+}$.²⁰

In contrast, complexes **2**-X display peaks in the preedge regions of their X-ray absorption spectra that have very similar energies (~7114.5 eV) and intensities (Figure 3 and Table 1). These energies are higher than those in iron(II) complexes,^{18,61} as would be expected because of the higher oxidation state, but the observed ~2-eV upshift makes these energies comparable to those of the corresponding transitions in Fe^{III}₂(μ-O) complexes,⁶¹ again reflecting the strong covalency of the Fe=O bond that mitigates the higher formal charge of the iron center.^{16,58–60} The preedge transitions, like the ligand-field bands, also involve 3d orbitals ($1s \rightarrow 3d$). In complexes with an Fe^{IV}=O unit, centrosymmetry is lost predominantly along the axis of the Fe=O bond, resulting in the mixing of $4p_z$ and $3d_z^2$ orbitals and making the $1s \rightarrow 3d_z^2$ transition the most intense in the preedge region. It is thus not surprising that the energy and intensity of this transition are not significantly affected by substitution of an equatorial ligand.⁶²

The thermal stabilities of the **2**-X series of complexes decrease in the following order: MeCN > CF₃CO₂[−] > Cl[−] > Br[−] > F[−] > CH₃CO₂[−]. From this progression, it is clear that the neutral MeCN has a stabilizing effect on the oxoiron(IV) unit and that replacing it with an anion has a destabilizing effect. The latter point may seem counterintuitive because anions may be expected to stabilize the iron(IV) center to the extent that they decrease the high positive charge. Indeed, the more basic the ligand, the greater is the instability. Complexes of the $[\text{Fe}^{\text{IV}}(\text{O})(\text{TMC})(\text{X})]^{2+/+}$ series also exhibit this trend in the replacement of the MeCN ligand trans to the oxo group in $[\text{Fe}^{\text{IV}}(\text{O})(\text{TMC})(\text{NCMe})]^{2+}$ with an anion.^{26,27} DFT calculations on the latter complex suggest that the axial MeCN ligand stabilizes the oxoiron(IV) unit by strengthening the Fe=O bond via a back-bonding-type interaction between the partially occupied π^* orbitals of the Fe=O unit and the empty π^* orbitals of the MeCN ligand.^{16,58–60} The loss of this key interaction upon anion substitution may account for the unexpected decrease in stability. Clearly, there is still much to learn regarding the electronic structure of these novel complexes and what factors affect their reactivity.

In summary, the Fe(TPA) complexes **2**-O₂CCF₃, **2**-Cl, and **2**-Br were generated by ligand substitution of **2**-NCMe and characterized as $S = 1$ Fe^{IV}=O complexes by a range of spectroscopic techniques, where striking similarities are observed in Mössbauer spectra and the XANES and EXAFS regions (for the Fe-N_{TPA} and Fe-O distances) of the X-ray absorption spectra, but distinct features are observed in the electronic absorption and EXAFS spectra (due to the

- (46) Mialane, P.; Nivorojkin, A.; Pratviel, G.; Azéma, L.; Slany, M.; Godde, F.; Simaan, A.; Banse, F.; Kargar-Grisel, T.; Bouchoux, G.; Sainion, J.; Horner, O.; Guilhem, J.; Tchertanova, L.; Meunier, B.; Girerd, J.-J. *Inorg. Chem.* **1999**, *38*, 1085–1092.
- (47) Klein Gebbink, R. J. M.; Jonas, R. T.; Goldsmith, C. R.; Stack, T. D. P. *Inorg. Chem.* **2002**, *41*, 4633–4641.
- (48) Goldsmith, C. R.; Jonas, R. T.; Cole, A. P.; Stack, T. D. P. *Inorg. Chem.* **2002**, *41*, 4642–4652.
- (49) Hazell, A.; McKenzie, C. J.; Nielsen, L. P.; Schindler, S.; Weitzer, M. *J. Chem. Soc., Dalton Trans.* **2002**, 310–317.
- (50) Balland, V.; Banse, F.; Anxolabéhère-Mallart, E.; Ghiladi, M.; Mattioli, T. A.; Philouze, C.; Blondin, G.; Girerd, J.-J. *Inorg. Chem.* **2003**, *42*, 2470–2477.
- (51) Davies, C. J.; Solan, G. A.; Fawcett, J. *Polyhedron* **2004**, *23*, 3105–3114.
- (52) Handley, D. A.; Hitchcock, P. B.; Leigh, G. J. *Inorg. Chim. Acta* **2001**, *314*, 1–13.
- (53) Lopez, J. P.; Heinemann, F. W.; Prakash, R.; Hess, B. A.; Horner, O.; Jeandey, C.; Oddou, J.-L.; Latour, J.-M.; Grohmann, A. *Chem.—Eur. J.* **2002**, *8*, 5709–5722.
- (54) Dick, S.; Weiss, A.; Wagner, U.; Wagner, F.; Grosse, G. *Z. Naturforsch., B: Chem. Sci.* **1997**, *52*, 372–384.
- (55) Mandon, D.; Nopper, A.; Litrol, T.; Goetz, S. *Inorg. Chem.* **2001**, *40*, 4803–4806.
- (56) Merkel, M.; Schnieders, D.; Baldeau, S. M.; Krebs, B. *Eur. J. Inorg. Chem.* **2004**, 783–790.
- (57) Breheret, A.; Lambeaux, C.; Menage, S.; Fontcave, M.; Dallemer, F.; Fache, E.; Pierre, J.-L.; Chautemps, P.; Averbusch-Pouchot, M.-T. *C. R. Acad. Sci., Ser. IIc: Chim.* **2001**, *4*, 27–34.
- (58) Zhang, Y.; Oldfield, E. *J. Am. Chem. Soc.* **2004**, *126*, 4470–4471.
- (59) Decker, A.; Solomon, E. I. *Angew. Chem., Int. Ed.* **2005**, *44*, 2252–2255.
- (60) Schöneboom, J. C.; Neese, F.; Thiel, W. *J. Am. Chem. Soc.* **2005**, *127*, 5840–5853.

- (61) Westre, T. E.; Kennepohl, P.; DeWitt, J. G.; Hedman, B.; Hodgson, K. O.; Solomon, E. I. *J. Am. Chem. Soc.* **1997**, *119*, 6297–6314.
- (62) This is, in fact, not the case for a similar series of $[\text{Fe}^{\text{IV}}(\text{O})(\text{TMC})(\text{X})]^{2+/+}$ complexes, where X[−] is trans to the oxo group (manuscript in preparation).

presence of chlorine and bromine scatterers). It seems noteworthy that, despite the weakened equatorial ligand field in **2**-Cl and **2**-Br, the energy gap between the $3d_{xz/yz}$ and $3d_{x^2-y^2}$ orbitals is still too large to allow spin crossover to the $S = 2$ state⁶⁵ that has been established for the oxoiron(IV) intermediate of TauD⁸ and the recently characterized $[\text{Fe}^{\text{IV}}(\text{O})(\text{H}_2\text{O})_5]^{2+}$ complex.⁶³ Nevertheless, this series represents the first examples of synthetic oxoiron(IV) complexes with a *cis*-X-Fe=O motif proposed for high-valent intermediates in the mechanisms of 2-oxoglutarate-dependent oxygenases (X = carboxylate),⁶⁴ isopenicillin N synthase (X = thiolate),²² and the recently discovered 2-oxoglutarate-dependent halogenases (X = halide).^{23,24} In the latter two cases, it is proposed that the anionic ligand coordinated *cis* to the oxo group (thiolate and chloride, respectively) is transferred to the carbon radical formed upon hydrogen-atom abstraction to form a C-S or C-Cl bond, instead of the C-OH bond usually expected in a rebound mechanism. Future work will focus on the oxidative reactivity of this series of $[\text{Fe}^{\text{IV}}(\text{O})(\text{TPA})(\text{X})]^+$ complexes as they relate to such enzymatic transformations.

(63) Pestovsky, O.; Stoian, S.; Bominaar, E. L.; Shan, X.; Münck, E.; Que, L., Jr.; Bakac, A. *Angew. Chem., Int. Ed.* **2005**, *44*, 6871–6874.

(64) Hausinger, R. P. *Crit. Rev. Biochem. Mol. Biol.* **2004**, *39*, 21–68.

(65) The crystal-field splitting between $3d_{xz/yz}$ and $3d_{x^2-y^2}$ is large and pushes the $S = 1$ state well below the $S = 2$ state (the energy difference at the optimized $S = 1$ geometry is 5000 cm^{-1} , which decreases to 1800 cm^{-1} after reoptimization in the high-spin state). The DFT calculations show that the equatorial ligand exchanges affect the energy gap between the lowest $S = 2$ state and $S = 1$ ground state by less than 1000 cm^{-1} . This energy difference leads to an estimated change in the zero-field-splitting parameter, D , of about 4 cm^{-1} , which is too small to be experimentally differentiated in a sample in which only 60–70% of the iron belongs to the oxoferryl species. For this reason, a high-field, variable-temperature Mössbauer study has not been carried out on complexes **2**-O₂CCF₃, **2**-Cl, and **2**-Br.

(66) Blasiak, L. C.; Vaillancourt, F. H.; Walsh, C. T.; Drennan, C. L. *Nature* **2006**, *440*, 368–371.

Note Added in Proof. A paper has recently appeared that reports the crystal structure of SyrB2, the halogenase involved in syringomycin biosynthesis, showing the coordination of a chloride ion in place of the more common carboxylate ligand in the enzymes with a 2-His-1-carboxylate facial triad.⁶⁶

Acknowledgment. This work was supported by grants from the National Institutes of Health (Grant GM-33162 to L.Q. and Grant EB-001475 to E.M.) and the Ministry of Science and Technology of Korea through the Creative Research Initiative Program (to W.N.) and fellowships from the Deutsche Forschungsgemeinschaft (to J.-U.R.) and the National Science Foundation (to A.S.). We thank William W. Brennessel of the University of Minnesota X-ray Crystallographic Facility for the crystal structure determinations of $[\text{Fe}_2(\mu\text{-O})(\mu\text{-OAc})(\text{TPA})_2](\text{OTf})_3 \cdot 2\text{H}_2\text{O}$ and $\text{NEt}_4[\text{FeBr}_4]$. XAS data were collected on beamlines 7-3 and 9-3 at the SSRL and beamline X9B at the NSLS, both supported by the U.S. Department of Energy and the National Institutes of Health. We thank Dr. Matthew J. Latimer at SSRL and Dr. Nebojsa S. Marinkovic at NSLS for their excellent technical support of our synchrotron experiments.

Supporting Information Available: Details of the crystal structure determinations of $[\text{Fe}_2(\mu\text{-O})(\mu\text{-OAc})(\text{TPA})_2](\text{OTf})_3 \cdot 2\text{H}_2\text{O}$ and $\text{NEt}_4[\text{FeBr}_4]$ (Tables S1, S2, S5, and S6 and Figures S1 and S6; PDF) and X-ray crystallographic files (CIF); ¹⁹F NMR spectra (Figure S2); Mössbauer spectra, Fe K-edge EXAFS spectra, and detailed EXAFS fitting protocols of all compounds (Figures S3 and S4 and Table S4); Fourier-transformed and -filtered EXAFS data and the best fit for duplicate **2**-Cl (Figure S5); XAS characterization of $\text{NEt}_4[\text{FeCl}_4]$ and $\text{NEt}_4[\text{FeBr}_4]$ (Figures S7–S9; PDF); and coordinates from DFT calculations (Table S7). This material is available free of charge via the Internet at <http://pubs.acs.org>.

IC060740U